Article   **Open Access**

Large dynamic range Shack-Hartmann wavefront sensor based on adaptive spot matching

Jiamiao Yang[1,2], Jichong Zhou[1], Lirong Qiu[3], Rongjun Shao[1], Linxian Liu[1,4] and Qiaozhi He[1,2,*] 🆔

Abstract

The Shack-Hartmann wavefront sensor (SHWS) is widely used for high-speed, precise, and stable wavefront measurements. However, conventional SHWSs encounter a limitation in that the focused spot from each microlens is restricted to a single microlens, leading to a limited dynamic range. Herein, we propose an adaptive spot matching (ASM)-based SHWS to extend the dynamic range. This approach involves seeking an incident wavefront that best matches the detected spot distribution by employing a Hausdorff-distance-based nearest-distance matching strategy. The ASM-SHWS enables comprehensive spot matching across the entire imaging plane without requiring initial spot correspondences. Furthermore, due to its global matching capability, ASM-SHWS can maintain its capacity even if a portion of the spots are missing. Experiments showed that the ASM-SHWS could measure a high-curvature spherical wavefront with a local slope of 204.97 mrad, despite a 12.5% absence of spots. This value exceeds that of the conventional SHWS by a factor of 14.81.

Keywords: Wavefront sensing, Large dynamic range, Shack-Hartmann sensor

Introduction

The Shack-Hartmann wavefront sensor (SHWS) is a noninterferometric technique for accurately measuring wavefronts. It provides fast measurement speed and strong resistance to environmental interference. The sensor has been widely used in various fields, such as astronomical observation, biological imaging, and ophthalmic diagnostics[1–10]. The SHWS setup comprises a microlens array (MLA) and image sensor. The MLA focuses the incident wavefront onto a series of spots on the sensor plane. After establishing the correspondence between each

spot and its respective microlens, the SHWS reconstruction algorithm calculates the displacements of the spots and determines the subaperture slopes of the wavefront. This method allows for accurate reconstruction of the wavefront. Conventional SHWS is limited by the maximum spot displacement, which is normally within the boundaries of a single microlens[11]. Consequently, this restriction limits the ability of the SHWS to measure wavefronts with substantial dynamic ranges and high slopes. Therefore, measuring wavefronts using conventional SHWS presents challenges[12].

Currently, various strategies are available for extending the dynamic range of SHWS. These strategies can be broadly categorized into hardware- and algorithm-based methods. Hardware-based methods involve physical modifications, such as shifting the position of the MLA or sensor, incorporating supplementary sensors or masks, and

Correspondence: Qiaozhi He (heqz1993@sjtu.edu.cn)
[1]School of Electronic Information and Electrical Engineering, Shanghai Jiao Tong University, Shanghai 200240, China
[2]Institute of Marine Equipment, Shanghai Jiao Tong University, Shanghai 200240, China
Full list of author information is available at the end of the article.
These authors contributed equally: Jiamiao Yang, Jichong Zhou

implementing liquid-filled MLAs[13–22]. These modifications provided more optical information, making it easier to match spots with larger displacements, thereby improving the dynamic range of the measurement. Nevertheless, these hardware modifications increase the system complexity and measurement duration, in contrast to algorithm-based methods that do not require changes to the current setup. Instead, spot-matching algorithms, including unwrapped algorithms[23], iterative extrapolation[24–28], neighborhood search[29], and spot sorting[30,31] were utilized. These algorithms can directly match spots that extend beyond the boundaries of the individual microlenses, thereby enabling the determination of larger displacements. This subsequently increases the dynamic range of the SHWS without incurring significant costs. However, the current spot-matching algorithms have two significant limitations. Firstly, they require prior knowledge of an initial correct correspondence. Second, their process typically involves progressively establishing spot correspondences on a local-to-global scale, which ultimately limits the spot-matching range to a few microlenses. Notably, these algorithms fundamentally adhere to a greedy approach and strive to achieve a global optimum by pursuing the local optima. Therefore, errors encountered during the search process can compromise the effectiveness of the search.

In this study, we present an SHWS based on adaptive spot matching (ASM) to measure wavefronts with a large dynamic range. The proposed ASM-SHWS formulates a cost function using a global matching approach to measure the divergence between the detected and estimated spot positions. This cost function then guides an efficient optimization algorithm to determine the optimal wavefront distribution that minimizes the divergence. Significantly, ASM-SHWS operates without requiring precise initial spot correspondences. This allows for one-to-one matching between every spot and microlens within the entire spot image. Consequently, there was a significant increase in the dynamic range. Additionally, owing to its global matching ability, ASM-SHWS maintains its ability to accurately match spots, even when some spots are absent. Our numerical simulations showed that ASM-SHWS can measure wavefronts with local slopes that exceed the conventional SHWS limit by a factor of 24.17. Moreover, even with half of the spots missing, ASM-SHWS can achieve both spot-matching and wavefront reconstruction. Furthermore, we constructed a physical SHWS prototype that can measure a spherical wavefront with a maximum slope of 204.97 mrad, even in the absence of 13.5% spots. This outcome surpasses that of conventional SHWS by a factor of 14.81.
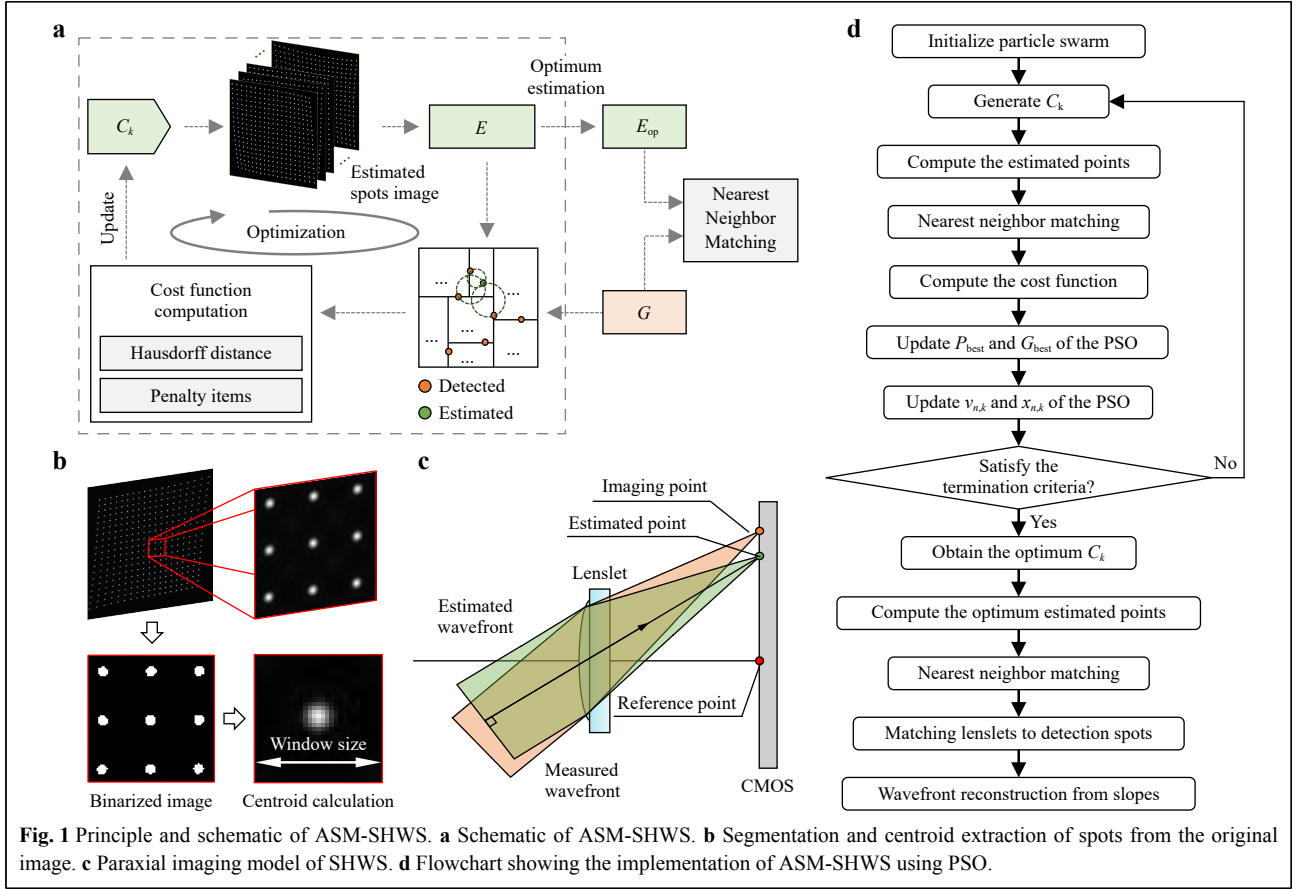
Principle of ASM-SHWS

Fig. 1 shows a schematic of the ASM-SHWS. An adaptive segmentation process based on nearest-neighbor matching was performed on the spot image acquired from the sensor, as shown in Fig. 1b. This process produces a set of detected points, labeled as G. Following this, a global matching optimization algorithm is used to accurately seek the incident wavefront that best approximates the distribution of the detected points in set G. To achieve spot matching, the estimated spot positions corresponding to each microlens are determined through the SHWS paraxial imaging model, depicted in Fig. 1c. The slopes within each microlens region were calculated to reconstruct the measured wavefront accurately (Fig. 1a).

The method for obtaining centroid coordinates from a spot image is illustrated in Fig. 1b. To account for the stark contrast in brightness between the spots and background, initial segmentation was conducted using Otsu's method[32]. This was followed by identification of the connected components of the spots, which clarified the distribution of each individual spot. The centroid extraction process allows the determination of the set of detected points, G.

To search for the optimal incident wavefront corresponding to the detected spots, the ASM-SHWS requires a characterization that describes the distribution of the incident wavefront. One technique involves characterizing the incident wavefront with Zernike coefficients C_k ($k = 1, 2, …, K$, where K stands for the number of Zernike coefficients). With the SHWS paraxial imaging model (Fig. 1c), the positions of the spots aligned with each microlens can be calculated by

$$\begin{cases} x_e^{(i)} = x_r^{(i)} + L \sum C_k \dfrac{\partial Z_k}{\partial x} \\ y_e^{(i)} = y_r^{(i)} + L \sum C_k \dfrac{\partial Z_k}{\partial y} \end{cases} \quad (1)$$

Here, $(x_e^{(i)}, y_e^{(i)})$ denotes the centroid coordinates of the i-th spot ($i = 1, 2, …, M$, and M is the total count of microlens within the MLA); $(x_r^{(i)}, y_r^{(i)})$ represents the imaging position of the i-th microlens optical axis on the sensor, which is previously calibrated and considered as a reference position; Z_k denotes the k-th Zernike polynomial term; and L denotes the distance between the MLA and sensor. To create the global matching cost function, the difference between the estimated and detected positions of the spots is initially calculated. To obtain a set of estimated points $E = \{(x_e^{(1)}, y_e^{(1)}), (x_e^{(2)}, y_e^{(2)}) …, (x_e^{(M)}, y_e^{(M)})\}$, the centroid coordinate of all spots is computed. Next, the Hausdorff distance d_H is calculated between sets E and G by

Fig. 1 Principle and schematic of ASM-SHWS. **a** Schematic of ASM-SHWS. **b** Segmentation and centroid extraction of spots from the original image. **c** Paraxial imaging model of SHWS. **d** Flowchart showing the implementation of ASM-SHWS using PSO.

$$
\begin{cases}
d_{\mathrm{FH}}(\boldsymbol{E},\boldsymbol{G}) = \sup_{e\in E} \inf_{g\in G} d(e,g) \\
d_{\mathrm{BH}}(\boldsymbol{E},\boldsymbol{G}) = \sup_{g\in G\in E} \inf_{e\in E} d(e,g) \\
d_{\mathrm{H}} = \max\{d_{\mathrm{FH}}, d_{\mathrm{BH}}\}
\end{cases}
\tag{2}
$$

Here, d_{FH} and d_{BH} denote the forward and backward Hausdorff distances, respectively; *sup* and *inf* denote the supremum and infimum, respectively; and $d(\cdot)$ quantifies the distance from a point $e \in \boldsymbol{E}$ to another $g \in \boldsymbol{G}$. When calculating d_{H}, it is necessary to establish point-to-point correspondences within sets $\boldsymbol{E}$ and $\boldsymbol{G}$, using the nearest-neighbor principle. Consequently, two K-dimensional (K-D) trees were created based on the two-dimensional distribution of these points. The points associated with nodes within the corresponding K-D trees are selected as neighboring points, effectively reducing the temporal complexity. A penalty term was included in the cost function to maintain the accuracy of optimization direction. This safeguards against a single point serving as the nearest neighbor for multiple points.

Fig. 1d depicts the employment of Particle Swarm Optimization (PSO) for optimizing the incident wavefront via the Zernike coefficients C_k. PSO emulates bird flocking behavior through particle representations to obtain an optimal solution[33]. This is achieved by the particle adaptation of position and velocity based on population and individual experience, facilitating the estimation of the incident wavefront. Unlike gradient-based methods, PSO does not require gradient information related to the cost function and possesses strong global search capability, thereby avoiding localized optimization traps. Assuming a swarm size of N, the initial positions $\boldsymbol{x_n}(0)$ ($n = 1, 2, …, N$) and initial velocities $\boldsymbol{v_n}(0)$ are assigned to the N particles, where $\boldsymbol{x_n}$ and $\boldsymbol{v_n}$ are K-dimensional vectors. Throughout each iteration, it is necessary to compute the cost function for every particle to update the positions and velocities of the particle swarm.

$$
\begin{cases}
v_{n,k}(t+1) = wv_{n,k}(t) + c_1 r_1 \left[P_{best} - x_{n,k}(t) \right] + \\
\qquad\qquad c_2 F_2 \left[G_{b\,\mathrm{bess}} - x_{n,k}(t) \right] \\
x_{n,k}(t+1) = x_{n,k}(t) + v_{n,k}(t+1)
\end{cases}
\tag{3}
$$

Here, $x_{n,k}(t)$ and $v_{n,k}(t)$ represent the values of the k-th dimension of $\boldsymbol{x_n}$ and $\boldsymbol{v_n}$ after t iterations. The inertia weight (w) controls the effect of the previous velocity on the current velocity. The cognitive coefficient (c_1) and social coefficient (c_2) determine the influence of the best-known positions of the particle (P_{best}) and swarm (G_{best}).

Generally, the inertia weight w is selected empirically within the range of 0–1, whereas the coefficients c_1 and c_2 are set within the range of 0–4. These coefficients were then multiplied by random numbers ($0 < r_1 < 1$ and $0 < r_2 < 1$) to introduce stochasticity.
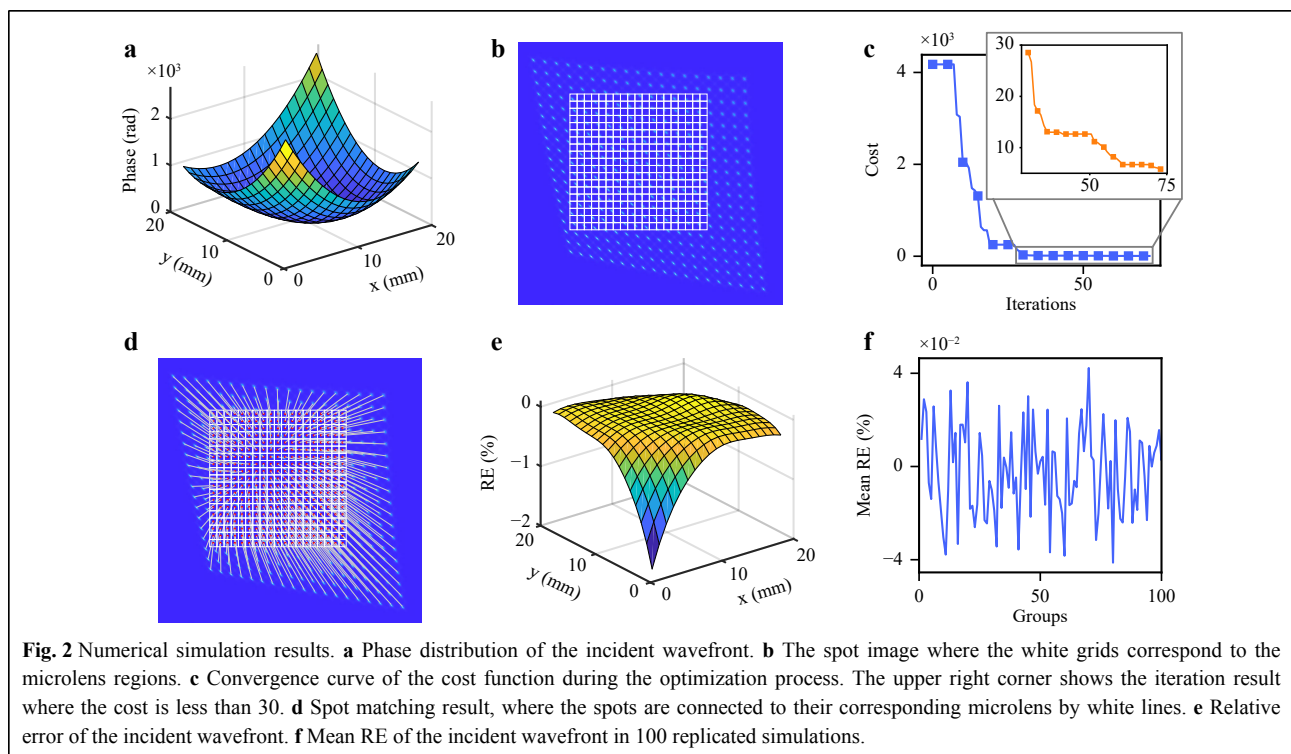
Using PSO, it is possible to attain the optimal estimation of C_k, which consequently makes it feasible to calculate the points within the estimated point set E. By establishing the correspondence between each point in set E and the microlenses, the correspondence between spots and microlenses can be deduced. Consequently, the slopes can be computed, and the incident wavefront can be reconstructed using a wavefront reconstruction algorithm such as modal decomposition or an iterative local reconstruction algorithm.

Numerical simulation

A thorough numerical simulation was performed to assess the effectiveness of the ASM-SHWS. The incident wavefront was generated by combining 15 Zernike polynomial terms and a random phase was produced by multiplying the Fourier spectrum of a random matrix by a two-dimensional Gaussian function[34]. The phase transfer function of the MLA was obtained using the thin-lens approximation. Subsequently, an SHWS model was developed using physical optics propagation, as described in our previous study[35]. The model utilized the angular

spectrum theory to imitate the propagation of the incident wavefront from the MLA to the sensor. The numerical simulation adopted various parameters including a wavelength of 632.8 nm, an assembly distance of 5.2 mm between the MLA and sensor, a microlens pitch of 150 μm, a lens radius of curvature of 2.54 mm, a 19×19 MLA, and a pixel size of 5 μm.
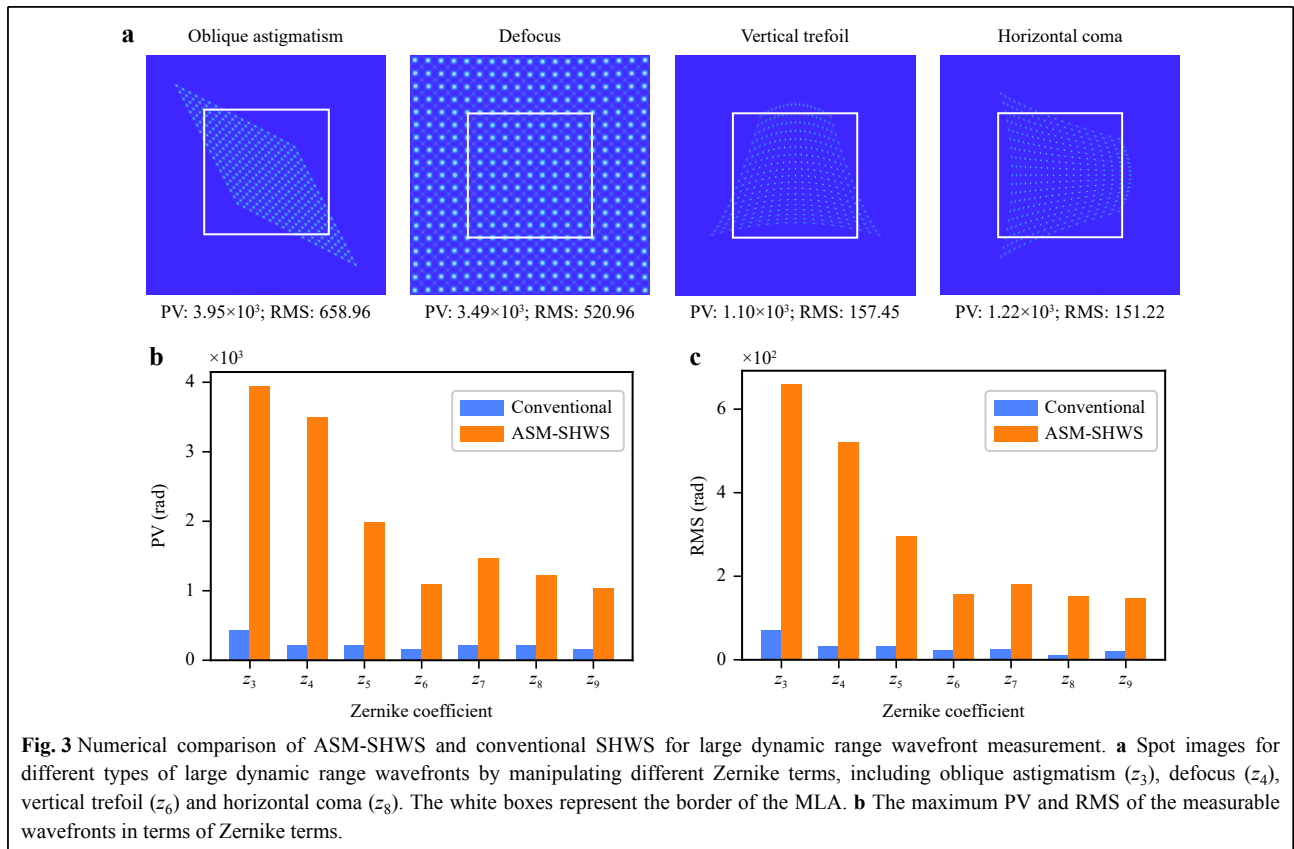
Fig. 2 shows the simulation results. It displays the phase distribution of the incident wavefront with a peak-to-valley (PV) value of 2617 rad. Fig. 2a, b show the corresponding spot image formed on the sensor. The most notable spot deviation was observed in the bottom-right corner, which exhibited horizontal and vertical displacements of 249.1 and 263.4 pixels, respectively. By contrast, under the same simulation parameters, the conventional SHWS could only achieve a maximum limit of 15 pixels for the horizontal and vertical displacements. The measurable threshold of the conventional SHWS for local slopes of the simulated incident wavefront was surpassed by a factor of 24.17. The convergence curve of the optimization cost function is shown in Fig. 2c. In our numerical simulations and subsequent experiments, we implemented the widely used default values of the coefficients $c_1 = c_2 = 1.49$ and inertia weight $w = 0.5$[36]. The swarm size was set to 100, and an initial search was performed for the first 15 Zernike polynomial coefficients. To begin the search, we initialized the Zernike coefficients to zero. Since the SHWS generally

Fig. 2 Numerical simulation results. **a** Phase distribution of the incident wavefront. **b** The spot image where the white grids correspond to the microlens regions. **c** Convergence curve of the cost function during the optimization process. The upper right corner shows the iteration result where the cost is less than 30. **d** Spot matching result, where the spots are connected to their corresponding microlens by white lines. **e** Relative error of the incident wavefront. **f** Mean RE of the incident wavefront in 100 replicated simulations.

measures the low-frequency components of the incident wavefront, we designated appropriate upper and lower bounds for the 15 Zernike coefficients, with the bounds for higher-order terms being notably smaller than those for lower-order terms. Specifically, we set the bounds of the C_1 to C_6 terms as $[-1, 1]$, C_7 to C_{10} as $[-0.1, 0.1]$, and C_{11} to C_{15} terms as $[-0.01, 0.01]$, with the coordinate units in millimeters. The termination criterion was set as the absence of duplicate matching points and a Hausdorff distance below 6 pixels. The efficacy of this criterion in establishing accurate matching relationships has been demonstrated through various tests. The dynamic spot matching process is depicted in Movie S1, and the final spot-matching result are shown in Fig. 2d. Fig. 2e shows the relative reconstruction error (RE) of the wavefront reconstructed using a modal wavefront reconstruction algorithm employing Zernike polynomials[37]. The distribution of the relative RE was indicated by $RE = (W_r - W_g)/PV$, where W_r and W_g represent the reconstructed and simulated incident wavefronts, respectively. The mean RE was 0.16% (Fig. 2e). The wavefront reconstruction procedure involved determining the slopes of the individual subwavefronts based on a paraxial approximation. An elevation in the paraxial

approximation and a centroid positioning error occurred with significant spot deviations. As a result, the RE increased owing to the steep slope of the edge subwavefront. To confirm the robustness of the ASM-SHWS, the procedure was replicated to generate and evaluate 100 sets of high dynamic range incident wavefronts. All 100 wavefronts displayed mean RE values below 0.20% (Fig. 2f). Therefore, the ASM-SHWS demonstrated its capability to achieve large dynamic range wavefront reconstruction with remarkable robustness.

To comprehensively evaluate the performance of the ASM-SHWS, we conducted numerical simulations to investigate various types of large dynamic range wavefronts by manipulating distinct Zernike terms, such as oblique astigmatism (z_3), defocus (z_4), vertical trefoil (z_6), and horizontal coma (z_8). We assessed the maximum measurable dynamic range of ASM-SHWS for these diverse wavefronts and the corresponding PV values for these wavefronts were 3.95×10^3, 3.49×10^3, 1.10×10^3, and 1.22×10^3 rad (Fig. 3a). Different factors can influence the measurement performance of the ASM-SHWS across various wavefronts. This is primarily limited by the receiving area of the image sensor for wavefronts generated by manipulating the defocus (z_4), whereas for

Fig. 3 Numerical comparison of ASM-SHWS and conventional SHWS for large dynamic range wavefront measurement. **a** Spot images for different types of large dynamic range wavefronts by manipulating different Zernike terms, including oblique astigmatism (z_3), defocus (z_4), vertical trefoil (z_6) and horizontal coma (z_8). The white boxes represent the border of the MLA. **b** The maximum PV and RMS of the measurable wavefronts in terms of Zernike terms.
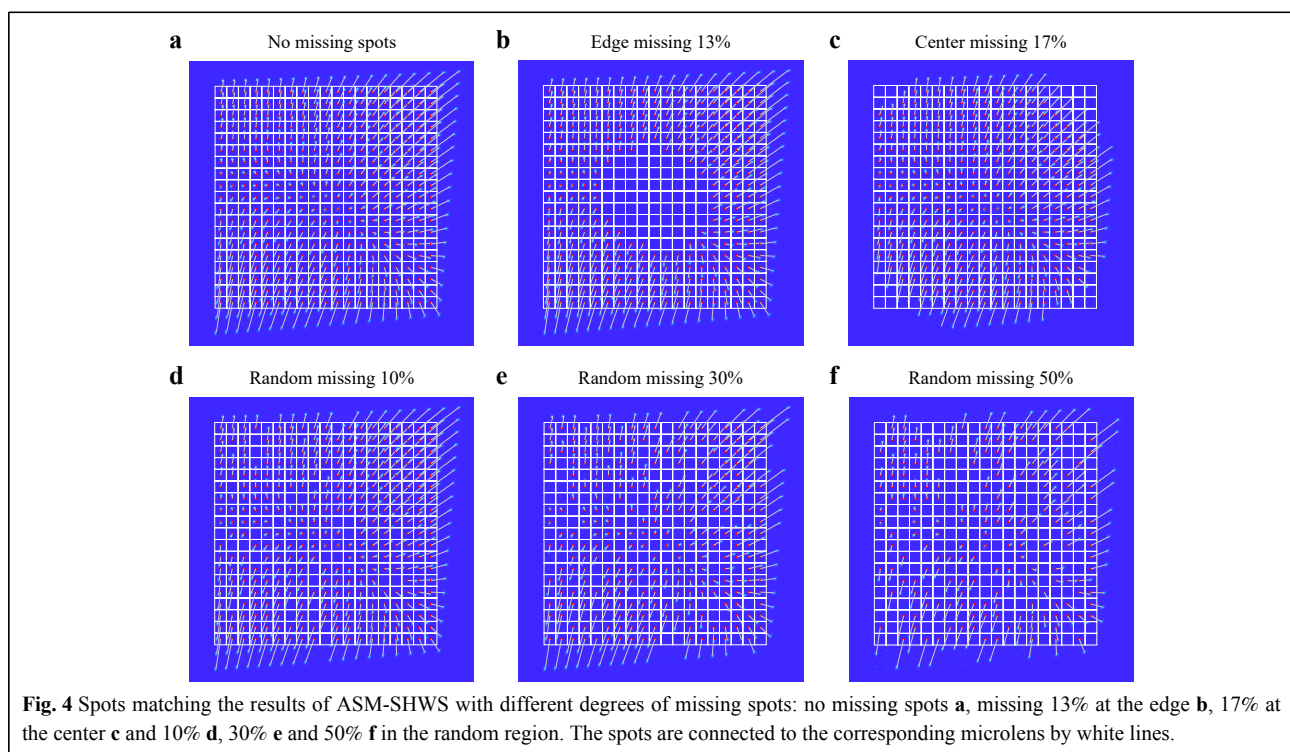
other wavefronts, it is restricted by the resolution of the sensor relative to adjacent spots. A comparison was conducted to determine the maximum dynamic range attainable by the ASM-SHWS and conventional SHWS for distinct wavefronts. Fig. 3b shows the maximum PV and root mean square (RMS) results. The results illustrated that the dynamic range of ASM-SHWS in terms of the PV and RMS exceeded that of the conventional SHWS by 16.21 times.
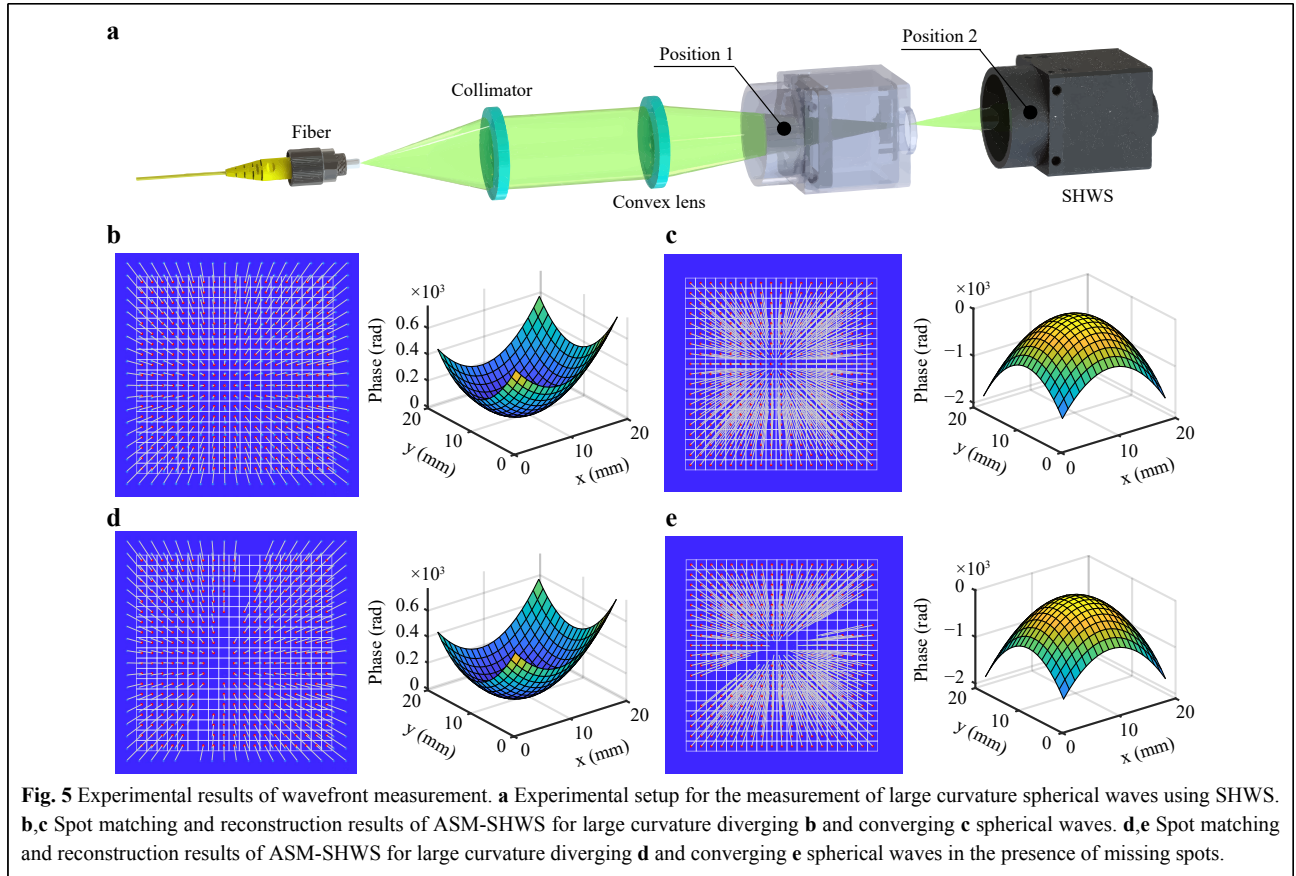
In an SHWS, a unique wavefront corresponds to a unique distribution of focal spots; conversely, a unique distribution of focal spots can be inversely mapped to a unique wavefront. Even when some focal spots were missing, the remaining spots retained some wavefront characteristics. On this basis, the ASM-SHWS is designed to search for the optimal incident wavefront that best matches the distribution of the detected spots rather than a specific positional relationship between the detected spots. As a result, the ASM-SHWS shows global matching capability in reconstructing wavefronts with a large dynamic range even in cases where partial spot images are obtained owing to factors such as occlusion, illumination fluctuations, or limited imaging areas. Fig. 4a shows the spot-matching results with no missing spots. By manually inspecting the spot positions, we confirmed the accurate alignment of the spots and microlenses in Fig. 4a, and used it as a reference to assess the matching accuracy when certain spots were missing. We simulated spot images with different degrees of missing spots, including 13% missing spots at the periphery, 17% missing spots at the center, and 10%, 30%, and 50% missing spots within random regions. As shown in Fig. 4b−f, under different missing spots scenarios, the ASM-SHWS consistently and accurately matched the remaining spots to their respective microlenses, maintaining the consistency of the reference matching relationship shown in Fig. 4a. Thus, ASM-SHWS shows great robustness to both localized and random instances of missing spots.

Experiment

To validate the practical accuracy of the ASM-SHWS, we constructed an SHWS sensor using an MLA (MLA150-7AR, Thorlabs, Inc.) and a CMOS sensor (IMX249, Sony, Corp.). The SHWS was characterized by a pixel size of 5.86 μm and a microlens pitch of 150 μm. The distance between the MLA and the CMOS sensor, calibrated using the spherical wavefront calibration method[38], was 5.42 mm. Given these parameters, the conventional SHWS demonstrated the ability to detect a maximum displacement of a single spot at 12.8 pixels, correlating to a maximum local slope of 13.84 mrad. The wavefront measurement setup is shown in Fig. 5a. The spherical wave emitted from the optical fiber was collimated and converged using a lens with a focal length of 100 mm. The SHWS was positioned

Fig. 4 Spots matching the results of ASM-SHWS with different degrees of missing spots: no missing spots **a**, missing 13% at the edge **b**, 17% at the center **c** and 10% **d**, 30% **e** and 50% **f** in the random region. The spots are connected to the corresponding microlens by white lines.

Fig. 5 Experimental results of wavefront measurement. **a** Experimental setup for the measurement of large curvature spherical waves using SHWS. **b,c** Spot matching and reconstruction results of ASM-SHWS for large curvature diverging **b** and converging **c** spherical waves. **d,e** Spot matching and reconstruction results of ASM-SHWS for large curvature diverging **d** and converging **e** spherical waves in the presence of missing spots.

both anterior and posterior to the focal point of the lens, allowing for the capture of highly curved converging and diverging spherical waves. The left sides of Fig. 5b, c show the spot images acquired at these positions. We reconstructed spherical waves using the ASM-SHWS and Zernike modal wavefront reconstruction algorithms. The reconstructed results after 41 and 47 iterations are shown on the right sides of Fig. 5b, c, respectively. Within our computing environment (MATLAB 2021a, CPU i7-10700), the computation time for the ASM-SHWS was 0.36 s and 0.41 s, respectively, which translates to ~8.8 ms per iteration. Subsequently, a spherical fitting procedure was performed on the reconstructed wavefronts, and their evaluation was quantified in terms of the Mean Relative Fitting Error (MRFE).

$$\text{MRFE} = \frac{1}{N} \sum_{n=1}^{N} \frac{|W_n - S_n|}{\text{PV}} \qquad (4)$$

Here, W_n and S_n denote the phase values of the *n*-th (*n* = 1, 2, 3, …, *N*) reconstruction point and the fitted sphere point, respectively. The MRFE values corresponding to the reconstructed diverging and converging spherical waves were 0.104% and 0.063%, respectively, compared with the

fitted sphere (Fig. 5b, c). Notably, for the reconstructed diverging spherical wave, the farthest matched spot exhibited displacements of 47.50 and 47.76 pixels along the *x* and *y* directions, respectively. It manifested a local slope of 72.83 mrad, exceeding the conventional SHWS limit by a factor of 5.26 (Fig. 5b). Similarly, for the converging spherical wave, the farthest displacements in the *x* and *y* directions were 131.48 and 136.59 pixels, respectively, along a local slope of 204.98 mrad, exceeding those of the conventional SHWS by a factor of 14.81 (Fig. 5c).

Finally, we experimentally tested the measurement capability of the ASM-SHWS in the presence of missing spots. To induce missing spots in the image, we partially occluded the effective aperture, resulting in the configuration shown on the left sides of Fig. 5d, e. To counteract the centroid calculation errors caused by partially occluded spots, we implemented a threshold during image segmentation that ensured that only spots with sizes exceeding the threshold were considered for matching and subsequent reconstruction calculations. Consequently, the ASM-SHWS achieved accurate spot matching for the remaining spots in the scenarios with 32

missing spots (8.9%) and 45 missing spots (12.5%). Under these conditions, the MRFE values associated with the reconstructed diverging and converging spherical waves were 0.010% and 0.048%, respectively, compared with the fitted sphere (Fig. 5d, e). With 8.9% missing spots, the farthest matched spot in the reconstructed diverging spherical wave had a displacement of 47.56 and 47.82 pixels along the x and y directions, respectively. It also had a local slope of 72.91 mrad, exceeding the conventional SHWS limit by a factor of 5.27 (Fig. 5d). Similarly, for the converging spherical wave and with 12.5% missing spots, the farthest displacement in the x and y directions was 131.43 and 136.62 pixels, respectively. This was accompanied by a local slope of 204.97 mrad, which exceeds the conventional SHWS limit by a factor of 14.81 (Fig. 5e).

Discussion and conclusion

In this study, we presented the ASM-SHWS as a solution for large dynamic range wavefront measurements. By using an optimizer to establish global spot-to-microlens correspondences, the ASM-SHWS effectively overcomes the limitations inherent in conventional SHWS, which limit the measurement of maximum spot displacements within a single microlens. To quantify the deviation between the spot positions extracted from the estimated wavefront and actual detected spot positions, the Hausdorff distance was used to formulate the optimization cost function. For wavefront continuity and dimensionality reduction during optimization, Zernike coefficients were used as optimization parameters, and the PSO algorithm was used for a fast global search to determine the incident wavefront that best matches the detected spot positions. Additionally, a penalty term for repeated matching was introduced into the cost function to ensure an accurate optimization direction. Through numerical simulations, we demonstrated that the ASM-SHWS achieves a maximum measurable local slope that exceeds that of the conventional SHWS by a factor of 24.17. Furthermore, ASM-SHWS was shown to be effective in accurately matching spots, even when up to 50% of the spots were missing. The experiments showed that the ASM-SHWS can measure a spherical wave with a local slope of 204.97 mrad, achieving a 14.81-fold improvement over the conventional SHWS limit, even with 12.5% missing spots.

The ability of the ASM-SHWS to measure large dynamic range wavefronts can be improved further. Current limitations in dynamic range measurement arise primarily from scenarios where the wavefront slope is too steep, resulting in spots that exceed the sensor's imaging range, and from cases where adjacent spots overlap, making it difficult to obtain accurate centroid coordinates during image segmentation. The former can be mitigated by enlarging the image sensor area, whereas the latter requires the application of more complex image segmentation algorithms. Furthermore, the ASM-SHWS is not limited to using Zernike polynomial coefficients to characterize the wavefront. Legendre polynomials and sub-wavefront slope values can also be used to further enhance the performance of the ASM-SHWS. The effectiveness of the ASM-SHWS is theoretically assured, provided that the measured wavefront maintains the necessary continuity and smoothness for the search of Zernike polynomial terms, along with accurate centroid extraction from the spot image. Moreover, on our current platform (MATLAB 2021a, CPU i7-10700), the algorithm achieves a processing speed of ~8.8 ms per iteration for a 19×19 array, typically converging within 100 iterations, resulting in a total runtime of less than 1 s. For a K-D tree, the time complexity of querying one point is $O(\log n)$, and when repeatedly searching for N points, the time complexity becomes $O(n\log n)$. Fortunately, the cost of PSO generally reaches a 90% reduction after approximately 25 iterations, with the estimated spots being very close to the detected spots. This proximity is sufficient for matching spots with microlenses using a nearest neighbor algorithm, and significantly reduces the measurement time for ASM-SHWS when the number of iterations is reduced to 25. Additionally, the implementation of advanced nearest neighbor matching algorithms, iterative optimization algorithms, parallel computing architectures, and efficient programming languages promises the realization of a large dynamic range and real-time SHWS.

The proposed ASM-SHWS offers substantial potential for improving the capabilities of SHWS in detecting complex wavefronts. Conventional SHWS often faces a trade-off between the dynamic range and resolution, that is, reducing the microlens pitch to increase resolution can lead to a reduction in the dynamic range. By contrast, the ASM-SHWS overcomes the limitation of the microlens pitch to the maximum measurable local slope. This advancement enables the measurement of complex wavefronts characterized by both a large dynamic range and high resolution. Furthermore, the ASM-SHWS excels at measuring wavefronts even with missing spots. This demonstrates its ability to handle complex measurement conditions. By effectively mitigating the disadvantages of resolution and dynamic range, the ASM-SHWS method expands the application scope of the SHWS, thus promoting progress in fields such as astronomical exploration and industrial inspection.

Rights and permissions

Author details
¹School of Electronic Information and Electrical Engineering, Shanghai Jiao Tong University, Shanghai 200240, China. ²Institute of Marine Equipment, Shanghai Jiao Tong University, Shanghai 200240, China. ³Beijing Key Lab for Precision Optoelectronic Measurement Instrument and Technology, School of Optoelectronics, Beijing Institute of Technology, Beijing 100081, China. ⁴School of Automation and Software Engineering, Shanxi University, Taiyuan 030006, China

Data availability
The data that support the findings of this study are available within the article.

Conflict of interest
The authors declare no conflicts of interest.

References
1. Lane, R. G. & Tallon, M. Wave-front reconstruction using a Shack–Hartmann sensor. *Applied Optics* **31**, 6902-6908 (1992).
2. Guo, Y. M. et al. Deep phase retrieval for astronomical Shack–Hartmann wavefront sensors. *Monthly Notices of the Royal Astronomical Society* **510**, 4347-4354 (2022).
3. Lan, B. et al. Distorted wavefront detection of orbital angular momentum beams based on a Shack–Hartmann wavefront sensor. *Optics Express* **30**, 30623-30629 (2022).
4. Andrade, P. P. et al. Estimation of atmospheric turbulence parameters from Shack–Hartmann wavefront sensor measurements. *Monthly Notices of the Royal Astronomical Society* **483**, 1192-1201 (2019).
5. Imperato, S. et al. Single-shot quantitative aberration and scattering length measurements in mouse brain tissues using an extended-source Shack-Hartmann wavefront sensor. *Optics Express* **30**, 15250-15265 (2022).
6. Brajones, J. M. et al. Highly sensitive Shack–Hartmann wavefront sensor: application to non-transparent tissue mimic imaging with adaptive light-sheet fluorescence microscopy. *Methods Protocols* **2**, 59 (2019).
7. Hu, L. J. et al. Learning-based Shack-Hartmann wavefront sensor for high-order aberration detection. *Optics Express* **27**, 33504-33517 (2019).
8. Holló, C. T. et al. Objective quantification and spatial mapping of cataract with a Shack-Hartmann wavefront sensor. *Scientific Reports* **10**, 12585 (2020).
9. Vacalebre, M. et al. Advanced optical wavefront technologies to improve patient quality of vision and meet clinical requests. *Polymers* **14**, 5321 (2022).
10. Park, J. H. et al. Perspective: wavefront shaping techniques for controlling multiple light scattering in biological tissues: toward *in vivo* applications. *APL Photonics* **3**, 100901 (2018).
11. Akondi, V. & Dubra, A. Shack-Hartmann wavefront sensor optical dynamic range. *Optics Express* **29**, 8417-8429 (2021).
12. Rocktäschel, M. & Tiziani, H. J. Limitations of the Shack–Hartmann sensor for testing optical aspherics. *Optics & Laser Technology* **34**, 631-637 (2002).
13. Lindlein, N., Pfund, J. & Schwider, J. Expansion of the dynamic range of a Shack-Hartmann sensor by using astigmatic microlenses. *Optical Engineering* **39**, 2220-2225 (2000).
14. Lindlein, N. & Pfund, J. Experimental results for expanding the dynamic range of a Shack-Hartmann sensor by using astigmatic microlenses. *Optical Engineering* **41**, 529-533 (2002).
15. Molebny, V. V. Scanning Shack-Hartmann wavefront sensor. Proceedings of SPIE 5412, Laser Radar Technology and Applications IX. Orlando, Florida, United States: SPIE, 2002.
16. Lee, W. W. , Lee, J. H. & Hwangbo, C. K. Increase of dynamic range of a Shack-Hartmann sensor by shifting detector plane. Proceedings of SPIE 5639, Adaptive Optics and Applications III. Beijing, China: SPIE, 2004.
17. Choo, H. & Muller, R. S. Addressable microlens array to improve dynamic range of shack–hartmann sensors. *Journal of Microelectromechanical Systems* **15**, 1555-1567 (2006).
18. Yoon, G. Y., Pantanelli, S. & Nagy, L. J. Large-dynamic-range Shack-Hartmann wavefront sensor for highly aberrated eyes. *Journal of Biomedical Optics* **11**, 030502 (2006).
19. Hongbin, Y. et al. A tunable Shack–Hartmann wavefront sensor based on a liquid-filled microlens array. *Journal of Micromechanics and Microengineering* **18**, 105017 (2008).
20. Martínez-Cuenca, R. et al. Reconfigurable Shack–Hartmann sensor without moving elements. *Optics Letters* **35**, 1338-1340 (2010).
21. Aftab, M. et al. Adaptive Shack-Hartmann wavefront sensor accommodating large wavefront variations. *Optics Express* **26**, 34428-34441 (2018).
22. Xu, H. F. & Wu, J. G. Extended-aperture Hartmann wavefront sensor

with raster scanning. *Optics Express* **29**, 34229-34242 (2021).

23. Pfund, J., Lindlein, N. & Schwider, J. Dynamic range expansion of a Shack-Hartmann sensor by use of a modified unwrapping algorithm. *Optics Letters* **23**, 995-997 (1998).

24. Groening, S. et al. Wave-front reconstruction with a Shack–Hartmann sensor with an iterative spline fitting method. *Applied Optics* **39**, 561-567 (2000).

25. Lundström, L. & Unsbo, P. Unwrapping Hartmann-shack images from highly aberrated eyes using an iterative B-spline based extrapolation method. *Optometry and Vision Science* **81**, 383-388 (2004).

26. Leroux, C. & Dainty, C. A simple and robust method to extend the dynamic range of an aberrometer. *Optics Express* **17**, 19055-19061 (2009).

27. Smith, D. G. & Greivenkamp, J. E. Generalized method for sorting Shack-Hartmann spot patterns using local similarity. *Applied Optics* **47**, 4548-4554 (2008).

28. Kumar, V. C. P. & Ganesan, A. R. Shack–Hartmann wavefront sensor with enhanced dynamic range and reference-free operation. *Optical Engineering* **61**, 054108 (2022).

29. Gao, Z. Y., Li, X. Y. & Ye, H. W. Large dynamic range Shack-Hartmann wavefront measurement based on image segmentation and a neighbouring-region search algorithm. *Optics Communications* **450**, 190-201 (2019).

30. Yu, L. et al. Novel methods to improve the measurement accuracy and the dynamic range of Shack–Hartmann wavefront sensor. *Journal of Modern Optics* **61**, 703-715 (2014).

31. Lee, J., Shack, R. V. & Descour, M. R. Sorting method to extend the dynamic range of the Shack-Hartmann wave-front sensor. *Applied Optics* **44**, 4838-4845 (2005).

32. Otsu, N. A threshold selection method from gray-level histograms. *IEEE Transactions on Systems, Man, and Cybernetics* **9**, 62-66 (1979).

33. Kennedy, J. & Eberhart, R. Particle swarm optimization. Proceedings of ICNN'95 - International Conference on Neural Networks. Perth, WA, Australia: IEEE, 1995.

34. Schott, S. et al. Characterization of the angular memory effect of scattered light in biological tissues. *Optics Express* **23**, 13505-13516 (2015).

35. Zhou, J. C. et al. Arbitrary wavefront uncertainty evaluation for the Shack–Hartmann wavefront sensor using physical optics propagation. *Applied Physics Letters* **123**, 071102 (2023).

36. Liang, J. J. et al. Comprehensive learning particle swarm optimizer for global optimization of multimodal functions. *IEEE Transactions on Evolutionary Computation* **10**, 281-295 (2006).

37. Dai, G. M. Modal wave-front reconstruction with Zernike polynomials and Karhunen–Loève functions. *Journal of the Optical Society of America A* **13**, 1218-1225 (1996).

38. Chernyshov, A. et al. Calibration of a Shack-Hartmann sensor for absolute measurements of wavefronts. *Applied Optics* **44**, 6419-6425 (2005).